

Anatomy of the AGN in NGC 5548

VII. *Swift* study of obscuration and broadband continuum variability

M. Mehdipour^{1,2}, J. S. Kaastra^{1,3,4}, G. A. Kriss^{5,6}, M. Cappi⁷, P.-O. Petrucci^{8,9}, B. De Marco¹⁰, G. Ponti¹⁰, K. C. Steenbrugge¹¹, E. Behar¹², S. Bianchi¹³, G. Branduardi-Raymont², E. Costantini¹, J. Ebrero^{14,1}, L. Di Gesu¹, G. Matt¹³, S. Paltani¹⁵, B. M. Peterson^{16,17}, F. Ursini^{8,9,13}, and M. Whewell²

¹ SRON Netherlands Institute for Space Research, Sorbonnelaan 2, 3584 CA Utrecht, The Netherlands
e-mail: M.Mehdipour@sron.nl

² Mullard Space Science Laboratory, University College London, Holmbury St. Mary, Dorking, Surrey, RH5 6NT, UK

³ Department of Physics and Astronomy, Universiteit Utrecht, PO Box 80000, 3508 TA Utrecht, The Netherlands

⁴ Leiden Observatory, Leiden University, PO Box 9513, 2300 RA Leiden, The Netherlands

⁵ Space Telescope Science Institute, 3700 San Martin Drive, Baltimore, MD 21218, USA

⁶ Department of Physics and Astronomy, The Johns Hopkins University, Baltimore, MD 21218, USA

⁷ INAF-IASF Bologna, via Gobetti 101, 40129 Bologna, Italy

⁸ Université Grenoble Alpes, IPAG, 38000 Grenoble, France

⁹ CNRS, IPAG, 38000 Grenoble, France

¹⁰ Max-Planck-Institut für extraterrestrische Physik, Giessenbachstrasse, 85748 Garching, Germany

¹¹ Instituto de Astronomía, Universidad Católica del Norte, Avenida Angamos 0610, Casilla 1280, Antofagasta, Chile

¹² Department of Physics, Technion-Israel Institute of Technology, 32000 Haifa, Israel

¹³ Dipartimento di Matematica e Fisica, Università degli Studi Roma Tre, via della Vasca Navale 84, 00146 Roma, Italy

¹⁴ European Space Astronomy Centre, PO Box 78, 28691 Villanueva de la Cañada, Madrid, Spain

¹⁵ Department of Astronomy, University of Geneva, 16 Ch. d'Ecogia, 1290 Versoix, Switzerland

¹⁶ Department of Astronomy, The Ohio State University, 140 W 18th Avenue, Columbus, OH 43210, USA

¹⁷ Center for Cosmology & AstroParticle Physics, The Ohio State University, 191 West Woodruff Ave., Columbus, OH 43210, USA

Received 11 November 2015 / Accepted 6 February 2016

ABSTRACT

We present our investigation into the long-term variability of the X-ray obscuration and optical-UV-X-ray continuum in the Seyfert 1 galaxy NGC 5548. In 2013 and 2014, the *Swift* observatory monitored NGC 5548 on average every day or two, with archival observations reaching back to 2005, totalling about 670 ks of observing time. Both broadband spectral modelling and temporal rms variability analysis are applied to the *Swift* data. We disentangle the variability caused by absorption, due to an obscuring weakly-ionised outflow near the disk, from variability of the intrinsic continuum components (the soft X-ray excess and the power law) originating in the disk and its associated coronae. The spectral model that we apply to this extensive *Swift* data is the global model that we derived for NGC 5548 from analysis of the stacked spectra from our multi-satellite campaign of 2013 (including *XMM-Newton*, *NuSTAR*, and *HST*). The results of our *Swift* study show that changes in the covering fraction of the obscurer is the primary and dominant cause of variability in the soft X-ray band on timescales of 10 days to ~5 months. The obscuring covering fraction of the X-ray source is found to range between 0.7 and nearly 1.0. The contribution of the soft excess component to the X-ray variability is often much less than that of the obscurer, but it becomes comparable when the optical-UV continuum flares up. We find that the soft excess is consistent with being the high-energy tail of the optical-UV continuum and can be explained by warm Comptonisation: up-scattering of the disk seed photons in a warm, optically thick corona as part of the inner disk. To this date, the *Swift* monitoring of NGC 5548 shows that the obscurer has been continuously present in our line of sight for at least 4 years (since at least February 2012).

Key words. X-rays: galaxies – galaxies: active – galaxies: Seyfert – galaxies: individual: NGC 5548 – techniques: spectroscopic

1. Introduction

The growth of supermassive black holes (SMBHs) in active galactic nuclei (AGN) is accompanied by powerful jets and/or winds of ionised gas. However, the association between the accretion and outflow phenomena in AGN is poorly understood, leading to important and outstanding questions in AGN science (see e.g. the review by Fabian 2012). Some of these questions are: which physical parameters regulate accretion and outflows; how is the energy budget distributed between accretion, outflows, and radiative output; how do they depend on the SMBH mass and accretion rate; what are the implications of the outflows on their host galaxies and beyond.

Because ionised outflows are ultimately powered and driven by energy released from the accretion process (e.g. Proga et al. 2000), their properties are expected to be related to the physical conditions and radiation spectra of the accretion disk and its associated higher-energy components. Determining the physical and ionisation structure, dynamics, and origin of the ionised outflows, as well as their role in shaping AGN spectra and variability, is crucial for advancing our knowledge of AGN. However, there are challenges before any general characterisation of the ionised outflows, their link to accretion, and their impact on their environment can be established.

One difficulty hampering our understanding of outflows is the uncertain nature of the observed X-ray spectral variability.

For example, both accretion-powered continuum emission and absorption by outflows may contribute to the observed spectral variability, and their disentanglement is challenging. Moreover, the origin of different intrinsic broadband components and their associations with each other are not fully understood, owing to the convolution of these components across wide energy bands. Monitoring the spectral variability of AGN at optical-UV-X-ray energies and incorporating both high-resolution spectroscopy and temporal analysis techniques is the most effective way of overcoming this challenge. Our extensive multi-wavelength campaign on the Seyfert 1 galaxy NGC 5548, introduced in [Mehdipour et al. \(2015, hereafter Paper I\)](#), provides a rare opportunity to determine the nature and origin of spectral variability in AGN and understand the physical processes which give rise to the formation of the AGN spectral energy distribution (SED).

From our campaign on NGC 5548, an exceptional kind of X-ray obscuring outflow was discovered at the core of this AGN by [Kaastra et al. \(2014, hereafter K14\)](#). In contrast to the commonly seen ionised winds at pc-scale distances from the SMBH (e.g. Mrk 509, [Kaastra et al. 2012](#)), the remarkable obscurer in this AGN is a new breed of weakly-ionised, yet high-velocity ($\sim 5000 \text{ km s}^{-1}$) outflowing wind close to the SMBH at distances of a few light days. It also extends into the broad-line region (BLR). This obscurer most likely originates from the accretion disk. Such obscuring disk winds have important implications for the launch of outflows and feedback dynamics in AGN. The obscuration shields gas from X-ray and extreme ultraviolet (EUV) radiation at the starting point of the wind, which is essential in order to drive away the wind using UV radiation in quasars (e.g. [Proga & Kallman 2004](#)). Bright and nearby Seyfert galaxies such as NGC 5548 are ideal laboratories for studying the mechanisms that drive powerful winds in the more luminous quasars (which are too faint in X-rays for a detailed spectral analysis), and can regulate the growth and co-evolution of SMBHs and their host galaxies.

The obscurer in NGC 5548 is partially covering the central X-ray emitting source (K14). Continuous and frequent monitoring with *Swift* over a few years enables us to trace the variability at optical-UV-X-ray energies, which is used to derive a precise characterisation of the continuum and obscuration variability. In order to obtain the continuum variability as far as possible into the UV energies, we make use of UV data from a *Hubble* Space Telescope (HST) Cosmic Origins Spectrograph (COS – [Green et al. 2012](#)) monitoring programme ([De Rosa et al. 2015](#)). Using the obscuration model of K14 and the broadband spectral model of Paper I (derived from stacked spectra of our campaign, including *XMM-Newton* and *NuSTAR*), we perform a broadband spectral and timing analysis of the *Swift* and HST COS data. This enables us to disentangle the X-ray variability caused by absorption (due to the obscurer) from different X-ray emission components originating from the accretion disk/coronal regions (the soft X-ray excess and the primary power-law), and study the nature and long-term variability of the obscuration and the optical-UV-X-ray continuum in NGC 5548.

The structure of this paper is as follows. Section 2 describes the *Swift* monitoring of NGC 5548, with an overview of the lightcurves and spectra. In Sect. 3 we present our broadband spectral modelling and examine the derived variability of the model parameters. In Sect. 4 we present our rms variability analysis of the X-ray and optical/UV lightcurves at different energies, and compare the observed rms spectra with the results of our broadband spectral modelling. We discuss all our findings in Sect. 5 and give concluding remarks in Sect. 6. In Appendix A

we show the relations between the *Swift* and HST COS optical/UV lightcurves at different energies.

The spectral analysis and modelling presented in this paper were done using the SPEX¹ package ([Kaastra et al. 1996](#)) v2.06.01. We also made use of tools in NASA’s HEASOFT² v6.14 package. The spectra shown in this paper are background-subtracted and are displayed in the observed frame. We use C-statistics for spectral fitting and give errors at 1σ (68%) confidence level. The redshift of NGC 5548 is set to 0.017175 ([de Vaucouleurs et al. 1991](#)). The adopted cosmological parameters for distance and luminosity computations in our modelling are $H_0 = 70 \text{ km s}^{-1} \text{ Mpc}^{-1}$, $\Omega_\Lambda = 0.70$ and $\Omega_m = 0.30$.

2. *Swift* monitoring of NGC 5548

Swift ([Gehrels et al. 2004](#)) has been extensively and frequently monitoring NGC 5548 over recent years, thanks to various observing programmes. On average there was an observation about every week in 2012, every two days in 2013 and every day in the first half of 2014. Apart from these data taken during the obscured epoch of NGC 5548, there were also a few observations taken in April–May 2005 and June–August 2007 when the source was unobscured. There were no *Swift* observations between August 2007 and February 2012. The total *Swift* observing time of NGC 5548 is 670 ks (up to 4 February 2015), of which 16 ks were taken in 2005, 21 ks in 2007, 62 ks in 2012, 327 ks in 2013, 211 ks in 2014 and 33 ks in 2015. The length of a *Swift* observation is 1–2 ks. In this study we have used all the *Swift* data taken up to 4 February 2015, when the regular *Swift* monitorings of NGC 5548 ended. The details of reduction and processing of the *Swift* data from the X-ray Telescope (XRT – [Burrows et al. 2005](#)) and the UV/Optical Telescope (UVOT – [Roming et al. 2005](#)), as well as other data from our campaign and also the observation logs, are presented in Paper I.

The UVOT observations of NGC 5548 have been mostly taken with the UVW2 filter in addition to other photometric filters. In a total of 668 UVOT observations recorded up to 4 February 2015, 90% of them had exposures taken with the UVW2 filter, 57% with UVW1, 56% with V, 52% with each B and U, and 50% with UVM2. This difference in coverage by the filters is due to various observing modes requested for UVOT and the filter-of-the-day selection at the time of the UVOT observations. The UVW2 filter provides the UV flux at shorter wavelengths (2030 Å) than other filters and demonstrates the clearest and largest variability seen by the instrument. Hence, it is useful for simultaneous timing analysis with the X-rays from XRT. During most of the 2013 and 2014 monitorings, all six primary UVOT filters were utilised.

For the purpose of determining the UV continuum variability at shorter wavelengths than that of UVOT, we used HST COS data of NGC 5548. The HST COS continuum data were incorporated together with *Swift* UVOT and XRT data in our broadband spectral modelling and rms variability analysis. We therefore selected only those COS observations which had contemporaneous *Swift* observations (separated by less than 24 h). The contemporaneous *Swift* and HST COS observations of NGC 5548 cover 120 days in total, 5 of which are from the multi-satellite campaign of 2013 (Paper I) and the remaining 115 days are from an optical/UV reverberation-mapping programme carried out in 2014 ([De Rosa et al. 2015](#)). The COS data consist of the observed continuum flux from five narrow wavelength bands

¹ <http://www.sron.nl/spex>

² <http://heasarc.nasa.gov/lheasoft>

(central wavelengths of 1158 Å, 1367 Å, 1462 Å, 1479 Å and 1746 Å), which are free of emission and absorption features over the wavelength range covered by the COS G130M and G160M gratings. More details about the optical/UV lightcurves (HST COS and UVOT) and their relations are given in Appendix A.

2.1. *Swift* lightcurves and spectra

Figure 1 shows the *Swift* lightcurves of NGC 5548 from 1 February 2012 to 4 February 2015, covering a range of 1100 days during the obscured epoch. The figure displays the soft (0.3–1.5 keV) and hard (1.5–10 keV) X-ray count rate fluxes from XRT and the corresponding X-ray hardness ratio, as well as the observed UV flux in the *UVW2* filter of UVOT. The X-ray hardness ratio (R) used here is defined as

$$R = (H - S)/(H + S) \quad (1)$$

where H and S are the count rate fluxes in the hard (1.5–10 keV) and soft (0.3–1.5 keV) bands of XRT, respectively.

The lightcurves of Fig. 1 display interesting features that one notices by eye before any analysis. It is evident that most of the time, the soft X-ray flux is well below the average level of the unobscured epoch (indicated by the horizontal dashed line in magenta), whereas in the hard band the flux is at similar (or higher) levels to the unobscured epoch. As explained in K14, the suppression of the soft X-rays in NGC 5548 is caused by an outflowing X-ray obscurer. The hardness ratio R , which is indicative of the soft X-ray absorption by the obscurer, shows the spectrum is continuously harder than during the unobscured epoch, when R was about 0.04. Thus, the *Swift* data indicate a long-lasting obscuration is occurring in NGC 5548. Furthermore, there appears to be a long-term gradual rise and decline of the hardness ratio in 2013 and 2014, pointing to a possible long-term variability of the obscurer. Interestingly, there is a significant positive correlation between the variability of the UV flux and that of the soft and hard X-ray bands (null hypothesis probability of $<10^{-10}$). Another feature is the anti-correlation between the X-ray hardness ratio and the UV flux: at some periods when the UV flux peaks, the hardness ratio dips (e.g. days 550–600 of the lightcurves), or when the UV dips, the hardness ratio peaks (e.g. days 740–790 of the lightcurves). This anti-correlation points to the soft X-ray excess component in NGC 5548 being linked to the UV continuum (explained in Sect. 3.1 and also Paper I), so that when the UV flux goes up, the source gets softer in the X-rays (i.e. the hardness ratio goes down). Following our spectral modelling in Sect. 3, the correlations are examined in Sect. 3.1.

Similar to the lightcurves, an overview of the *Swift* X-ray spectra also exhibits the effects of obscuration and its variability. Figure 2 shows examples of XRT spectra taken at different epochs highlighting interesting spectral changes. The observed spectral variability can be due to a combination of the continuum and the obscuration variability, which produces a characteristic dip and curvature in the soft X-ray band. Compared to the unobscured spectrum, which still includes absorption by a traditional warm absorber (Steenbrugge et al. 2005), the dominant absorption effects by the obscurer are obvious in the 2013 and 2014 obscured spectra. However, in the low-flux obscured spectrum, which overlaps with our summer (22 June to 1 August) 2013 *XMM-Newton* campaign, the absorption by the obscurer appears stronger than in later observations taken in spring 2014. In Sect. 3, we investigate the origin of these observed features in the *Swift* lightcurves and spectra of NGC 5548 by modelling

the variability of the obscurer and the underlying broadband continuum.

The exposure time of a *Swift* observation is short (1–2 ks), so in order to improve the signal-to-noise of the XRT spectra and hence improve constraints on the parameters of our spectral model, time-averaged stacked spectra were created. By examining the *Swift* data of NGC 5548, we found that ten days is the optimum interval for stacking, providing XRT spectra with both sufficient statistics and near continuous equally time-binned datasets. Therefore, in our broadband spectral modelling of Sect. 3, the *Swift* XRT and UVOT data, as well as the HST COS continuum data, were time-averaged over ten days. Similarly, in our temporal rms variability analysis of Sect. 4, a time sampling bin size of ten days was selected.

3. Broadband spectral modelling of the *Swift* data

We modelled the *Swift* data of NGC 5548 using the broadband continuum model derived in Paper I, which was obtained from modelling of the stacked simultaneous data (*XMM-Newton*, NuSTAR, INTEGRAL, HST COS and two ground-based optical observatories) from our campaign of summer 2013. In this global model of the SED, which covers energies from near-infrared (NIR) (wavelength of 8060 Å) to hard X-rays (200 keV), we take into account various non-intrinsic emission and absorption processes along our line of sight, which are: Galactic reddening, host galaxy stellar emission, BLR and narrow-line region (NLR) emission lines, blended Fe II and Balmer continuum, Galactic interstellar X-ray absorption, the traditional warm absorber, soft X-ray emission lines and finally absorption by the obscurer (see Paper I for more details). The parameters of these model components, except those of the obscurer, have been kept fixed throughout our modelling of the *Swift* data.

The broadband continuum of our model consists of a Comptonisation component for the NIR-optical-UV continuum and the soft X-ray excess, and a power-law component for the primary hard X-ray continuum, plus a neutral X-ray reflection component. As justified in Paper I, warm Comptonisation is a feasible and likely explanation for the soft X-ray excess emission in NGC 5548. This model can also explain the apparent correlation between the soft X-ray and UV flux (Sect. 2.1). In this model the thermal seed photons from the disk are up-scattered in a warm, optically thick corona to produce the soft excess emission (see e.g. Done et al. 2012). So the NIR-optical-UV continuum of NGC 5548 is composed of a single thermal Comptonised component (comt in SPEX), which also produces the soft X-ray excess (Paper I). The up-scattering Comptonising plasma was set to have a disk geometry and the initial values for its parameters were fixed to those obtained from the stacked 2013 spectra in Paper I: temperature of the seed photons $T_{\text{seed}} = 0.80$ eV, electron temperature of the plasma $T_e = 0.17$ keV, optical depth $\tau = 21.1$ with comt normalisation of 6.0×10^{55} photons s^{-1} keV^{-1} .

In addition to the Comptonised soft excess component, the primary hard X-ray continuum was modelled with a cut-off power law (pow in SPEX), which mimics the spectral emission produced by inverse Compton scattering in an optically thin ($\tau \sim 1$), hot ($T_e \sim 100$ keV) corona (e.g. Sunyaev & Titarchuk 1980; Haardt & Maraschi 1993). The cut-off power law is known to provide a reasonable approximation for the hot Comptonisation spectrum (e.g. Petrucci et al. 2000). The weak reflection component in NGC 5548 was also included in our modelling, which is consistent with being constant and produced

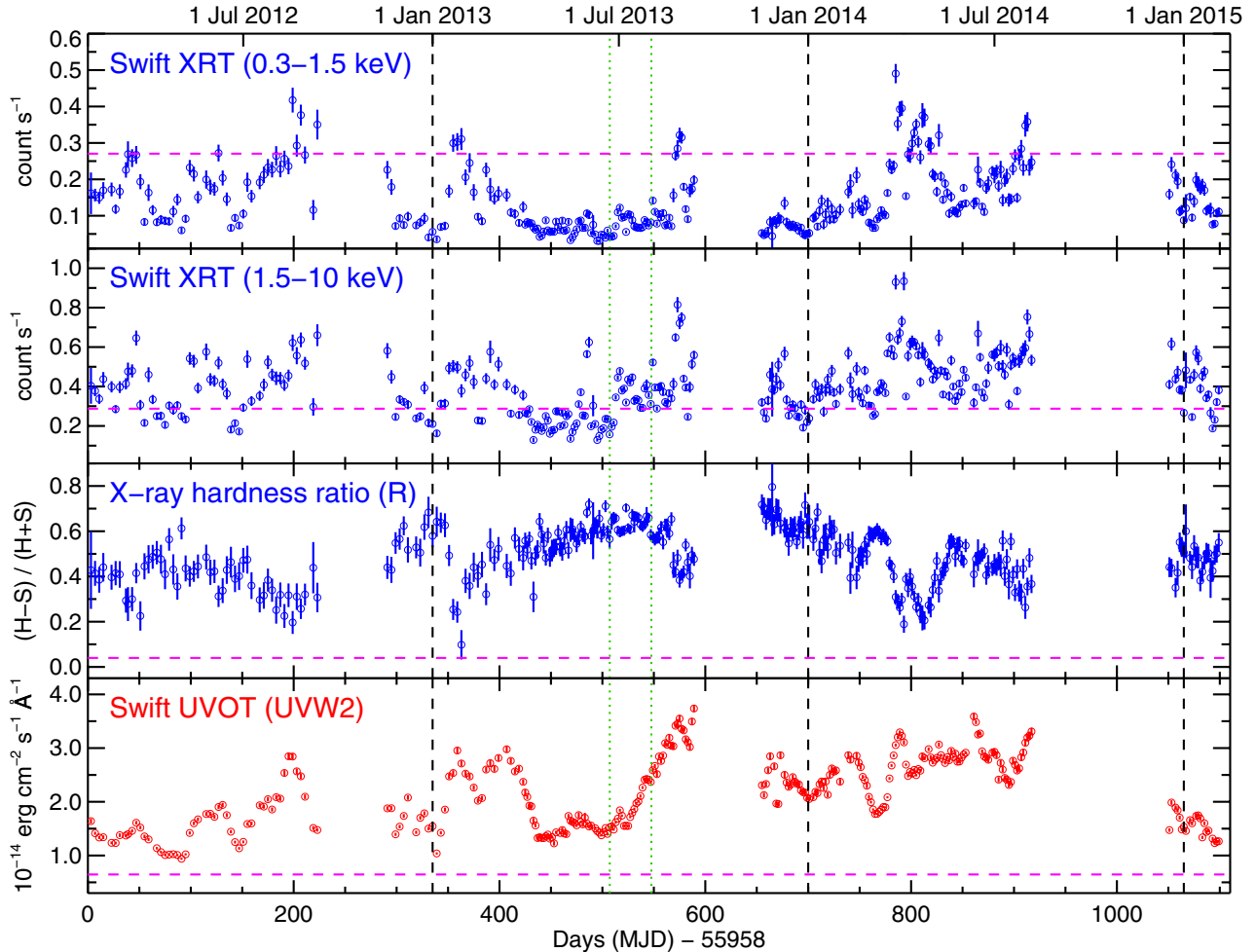


Fig. 1. *Swift* lightcurves of NGC 5548 from 1 February 2012 to 4 February 2015, during which the X-ray source is obscured. The data are displayed with bin sizes of two days for clarity of presentation. The vertical dotted lines in green indicate the interval of our summer 2013 *XMM-Newton* campaign. The vertical dashed lines in black indicate the start of each year for reference. The horizontal dashed lines in magenta represent the averages from *Swift* observations in 2005 and 2007, when the X-ray source was unobscured. The panels are described in Sect. 2.1.

in neutral, distant material (Ursini et al. 2015; Cappi et al. 2016, Paper VIII). Since we can only fit *Swift* XRT data up to 10 keV, all the parameters of the reflection spectrum and the high-energy exponential cut-off of the power law (400 keV), which are not in the XRT bandpass, have been fixed to those reported in Paper I. For the reflection component, we used the refl model in SPEX, which computes the reflected continuum and the corresponding Fe $K\alpha$ line from a constant density X-ray illuminated atmosphere. At low energies, the power law was smoothly broken before overshooting the energies of the seed photons from the disk as described in Paper I.

The obscurer model, first described in K14, consists of two photoionised absorption components, each modelled with an xabs component in SPEX. The xabs model calculates the transmission through a slab of photoionised gas, where all ionic column densities are linked in a physically consistent fashion through the Cloudy (Ferland et al. 1998) photoionisation model. The parameters of an xabs component are the ionisation parameter (ξ), the equivalent hydrogen column density (N_{H}), the covering fraction C_{f} of the absorber, its flow v and turbulent σ_v velocities. The ionisation parameter ξ (Tarter et al. 1969) is defined as $\xi \equiv L / n_{\text{H}} r^2$, where L is the luminosity of the ionising source over the 1–1000 Ryd (13.6 eV to 13.6 keV) band in erg s^{-1} , n_{H} the hydrogen density in cm^{-3} and r the distance

between the ionised gas and the ionising source (in cm). In this time-averaged model of the obscurer, component 1 covers about 86% of the central X-ray emitting region, with $\log \xi = -1.2$ and $N_{\text{H}} = 1.2 \times 10^{22} \text{ cm}^{-2}$. Component 2 of the obscurer covers 30% of the X-ray source and is almost neutral ($\log \xi = -4.0$) with $N_{\text{H}} = 9.6 \times 10^{22} \text{ cm}^{-2}$. We shall refer to component 1 and 2 as warm and cold phases of the obscurer, respectively. For the unobscured epoch (2005 and 2007 *Swift* data), the obscurer components were excluded from our model by setting C_{f} of both obscurer components to zero. During the obscured epoch (February 2012 onwards) we set the initial parameters of the obscurer to those of K14 and Paper I. Since the obscurer is located between the central ionising source and the traditional warm absorber, it prevents some of the ionising EUV and X-ray radiation from reaching the warm absorber. Thus the different phases of the warm absorber become less ionised (de-ionised) and induce more X-ray absorption than when NGC 5548 was unobscured. In our modelling of the obscured *Swift* data we used the de-ionised warm absorber model obtained by K14, which consists of six phases (xabs) of photoionisation. For the unobscured *Swift* data from 2005 and 2007, the warm absorber would have been exposed to a normal unobscured ionising SED, whose parameters are derived by K14 and used in our modelling here.

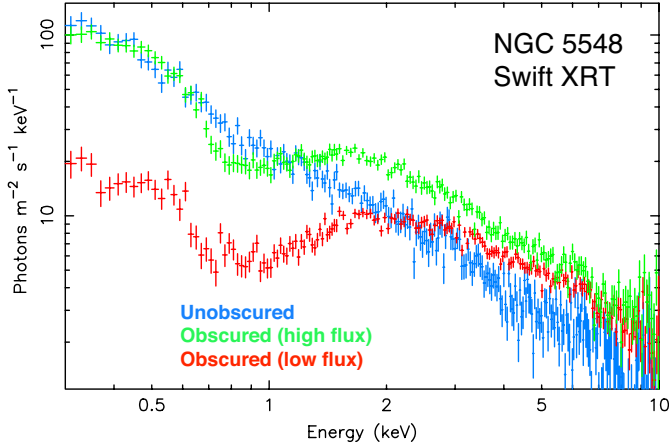


Fig. 2. Examples of NGC 5548 *Swift* XRT spectra taken at different epochs. The unobscured spectrum (shown in blue) corresponds to the archival 2005 and 2007 data. The low-flux obscured spectrum (shown in red) is produced from observations taken between 22 June and 1 August 2013 (56 465–56 505 in MJD). The high-flux obscured spectrum (shown in green) corresponds to observations taken between 20 March and 29 April 2014 (56 736–56 776 in MJD). The visible spectral changes are indicative of variability induced by both the obscurer and the underlying continuum emission.

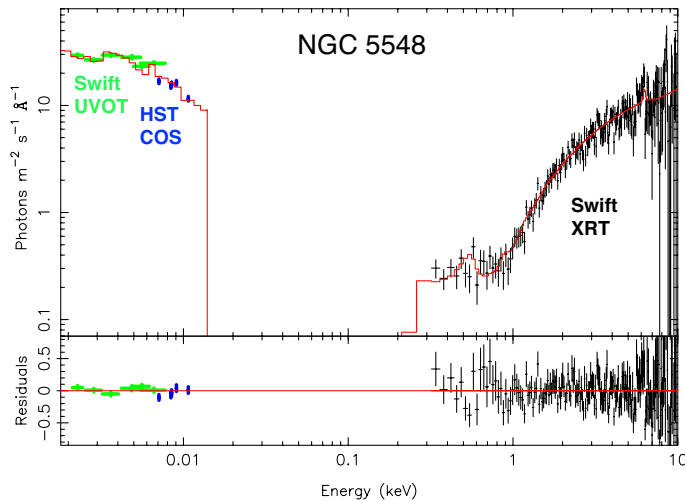


Fig. 3. Typical example of one set of observed optical/UV (*Swift* UVOT and HST COS) and X-ray (*Swift* XRT) spectra of NGC 5548, which were fitted with the broadband spectral model described in Sect. 3. The UVOT fluxes are from six photometric filters and the HST COS fluxes are from five narrow energy bands in the UV continuum. Residuals of the fit, defined as (observed–model)/model, are shown in the bottom panel. The displayed data are from a 10-day bin period between 2–12 March 2014.

We started our spectral fitting procedure by first fitting the 3.0–10 keV part (which is almost unabsorbed) of each of the 93 XRT spectra by freeing the Γ and normalisation of the power-law component (pow). The power-law parameters were then temporarily kept frozen while the whole 0.3–10 keV XRT spectrum, and optical/UV (UVOT and HST COS) data were fitted by freeing the normalisation of the Comptonisation (comt) component. This was then followed by freeing the covering fraction of the warm phase of the obscurer (C_f), which from the analysis of *XMM-Newton* spectra by Di Gesu et al. (2015) and Ursini et al. (2015) is found to be significantly variable. Then, the power-law parameters were freed again to obtain a best-fit.

Next, we tested whether fitting other parameters of the obscurer improves our spectral fits. By freeing the covering fraction of the cold phase of the obscurer (which has a much lower value than that of the warm phase), our fits did not improve and the covering fraction often became unconstrained. We thus kept the covering fraction of the cold phase of the obscurer fixed to its initial value throughout our modelling as XRT spectrum is much less sensitive to this weaker phase than the more prominent warm phase of the obscurer. We discuss the significance of this assumption in Sect. 5.1. Hereafter, obscurer C_f refers to the covering fraction of the warm phase of the obscurer. We then checked whether freeing the column densities N_H of the obscurer components improves our fits. However, we did not observe any significant improvement in our fits and the N_H values became weakly constrained. We then tried another scenario, in which the covering fractions of the components were fixed to their initial values, and instead their N_H were fitted. But in this case, for most datasets we obtained a worse fit. So in our modelling we have kept N_H of the obscurer components fixed to the best-fit values obtained by K14 from the stacked summer 2013 spectra, and allowed C_f of the obscurer to vary. In Sect. 4 we will show that the rms variability produced by changes in the C_f of the obscurer is indeed consistent with the observed rms spectra of NGC 5548.

Next, we checked for possible variability of T_{seed} , T_e and τ of the comt component, and whether freeing these parameters improve our broadband spectral fits. We found that freeing T_{seed} helps in making a better fit to the optical/UV (UVOT and HST COS) data in some observations, particularly when the UV flux had a flare-up. We thus left T_{seed} as a free parameter in our modelling. On the other hand, freeing T_e and τ did not make a statistically significant difference to our fits. Therefore, we froze T_e and τ to avoid unnecessary free parameters and kept them fixed to their initial values. Indeed varying the normalisation and T_{seed} of comt is sufficient to provide a good fit to the optical/UV data and the soft X-ray excess in all our datasets. At the final step, the goodness of our fits was re-examined. In all the observations, the data were well fitted with good C-statistic values. In addition to examining the C-statistic output, the quality of our best-fits was also inspected visually at the end to make sure all optical/UV and X-ray data were properly fitted.

In Fig. 3, we show a typical example of one set of *Swift* (XRT and UVOT) and HST COS spectral data (time-averaged over ten days), together with its best-fit broadband model. To find out how individual model spectral components contribute to the global broadband model used in this paper, see Figs. 5 and 10 in Paper I. In total, a series of 93 sets of such stacked data were fitted using a batch processing script incorporating our broadband model described above. Figure 4 illustrates the variability of the fitted parameters of our broadband spectral model of the continuum and obscuration. The obtained and expected C-statistic values (see the SPEX manual for their definitions) are also provided in this figure. Additionally, the X-ray hardness ratio R and the observed flux in the UVOT *UVW2* filter are also displayed for comparison with the derived parameters. We examine the variability of the model parameters of Fig. 4 in Sect. 3.1.

3.1. Long-term variability of the obscuration and continuum parameters

The time-series of model parameters in Fig. 4 exhibit interesting features, which we examine here. The variability trend of the obscurer covering fraction C_f is very similar to that of the X-ray hardness ratio R measured with *Swift* XRT. For correlation

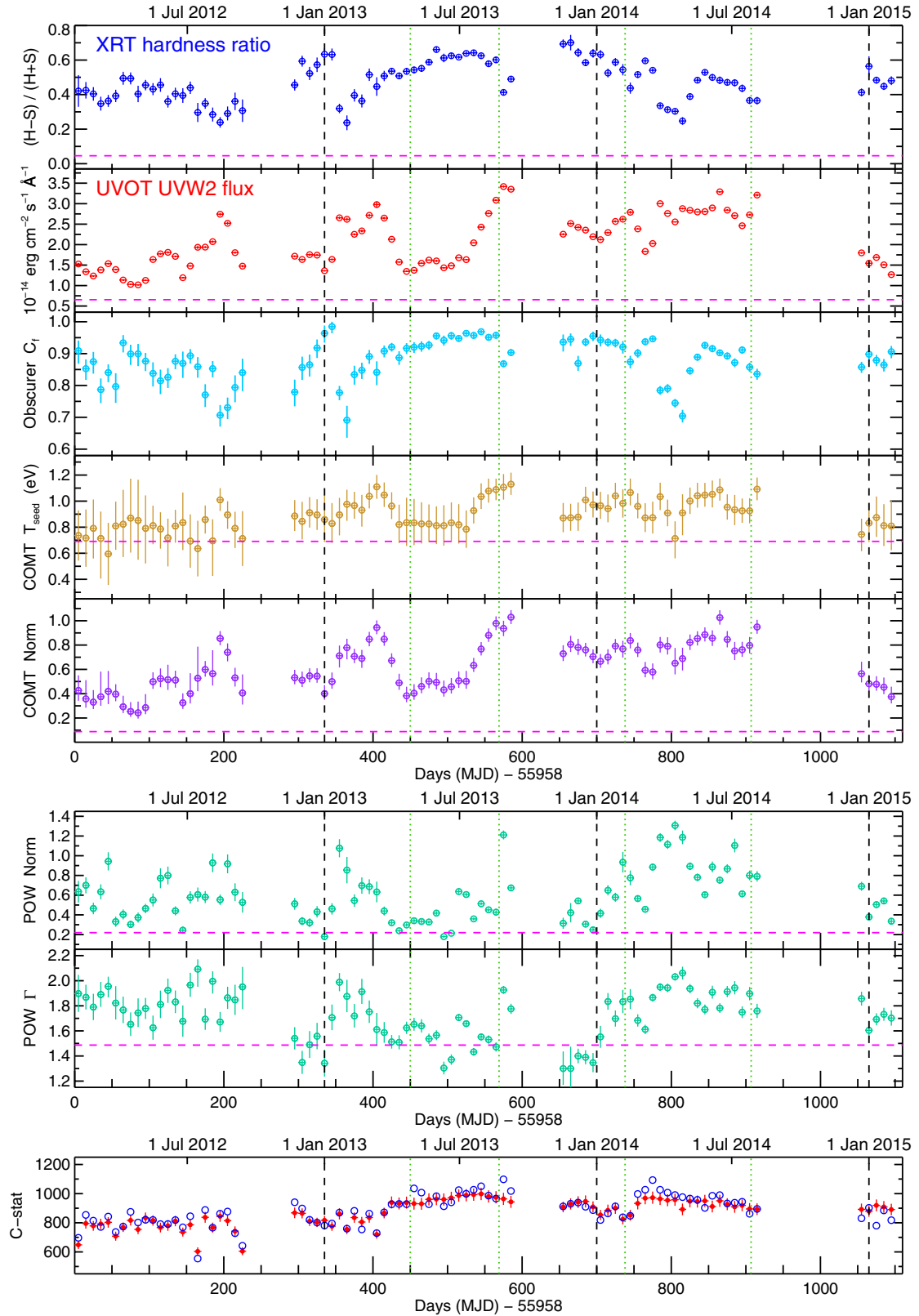


Fig. 4. Variability of the parameters derived from broadband spectral modelling of *Swift* and HST COS data of NGC 5548 in Sect. 3. The X-ray hardness ratio R and the *UVW2* flux are also displayed on the *top two panels* for comparison. On the vertical axis of each panel the name of the corresponding parameter is given. The normalisation of the warm Comptonisation (comt) component (modelling the optical/UV continuum and the soft X-ray excess) is shown in units of 10^{56} photons $\text{s}^{-1} \text{keV}^{-1}$. The power-law (pow) normalisation is in 10^{52} photons $\text{s}^{-1} \text{keV}^{-1}$ at 1 keV. In the *bottom panel*, the goodness of the fits are shown, with blue open circles indicating the obtained C-stat and the filled red circles indicating the expected C-stat with its rms uncertainties. The range of the above time-series is from 1 February 2012 to 4 February 2015. The vertical dotted lines in green indicate two interesting periods in 2013 and 2014, which were selected for the temporal variability analysis of Sect. 4 and production of rms spectra in Fig. 8. The vertical dashed lines in black indicate the start of each year for reference. The horizontal dashed lines in magenta represent the averages from previous years (2005 and 2007 *Swift* data from the unobscured epoch) derived in this work with the same model.

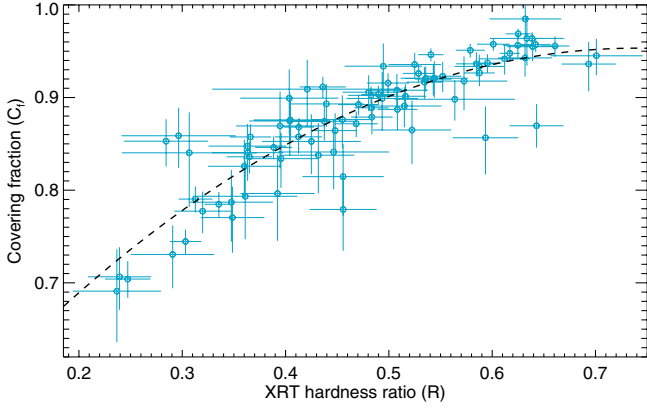


Fig. 5. Relation between the covering fraction (C_f) of the obscurer and the observed XRT hardness ratio (R). The data have been fitted with Eq. (2), shown in dashed black line, as described in Sect. 3.1.

between C_f and R in our obscured sample size of 85, the Pearson correlation coefficient is $r = 0.858$. This gives a negligible null hypothesis probability of $p_{\text{null}} < 10^{-10}$. Thus, there is a strong positive correlation between C_f and R . In Fig. 5, we have plotted the obscurer C_f versus R . The data are well fitted with a quadratic function, given by

$$C_f = 0.46 + 1.34 R - 0.91 R^2, \quad \text{for } 0.7 \leq C_f \leq 1. \quad (2)$$

We note that a quadratic function is preferred over a linear one as it provides a better description of the data at both low and high extremes.

Since the start of the *Swift* monitoring in February 2012, the C_f time-series in Fig. 4 shows that at no point in time the central X-ray source became unobscured. The obscuration has been continuously present, with its covering fraction varying over time between 0.70 and 0.98. A useful aspect of the relation in Fig. 5 is that by simply measuring the hardness ratio R from *Swift* observations, one roughly knows the covering fraction of the obscurer without any modelling. We note that apart from the clear relation between C_f and R , there is also a weaker anti-correlation ($p_{\text{null}} \approx 0.05$) between these parameters and the *UVW2* flux when it flares up (steep continuous increase over 1–2 months). The increase in the UV flux is accompanied by a decrease in the covering fraction of the obscurer. We note that this anti-correlation contributes in producing the scatter observed between the C_f and R relation in Fig. 5. We further discuss these correlations and the obscurer C_f variability in Sect. 5.

The time-series of Fig. 4 also show a clear link between the variability of the *UVW2* flux and the parameters of the warm Comptonisation component (comt). As this is the component which fits the optical/UV continuum and the soft X-ray excess, there is naturally a tight correlation between the normalisation of comt (N_{comt}) and the UV flux. However, there also appears to be a correlation between the *UVW2* flux and T_{seed} of comt when the *UVW2* flux flares up. However, at other times, T_{seed} is more or less unchanged within its larger error bars as N_{comt} alone is sufficient to fit the optical/UV variability in most observations. In Fig. 6, the relation between the *UVW2* flux and T_{seed} (top panel), and normalisation of comt (bottom panel) are shown. For a sample size of 90 (which have *UVW2* data in our spectral modelling), the correlation coefficient between F_{UVW2} and T_{seed} is $r = 0.810$, and between F_{UVW2} and N_{comt} is $r = 0.981$, with both giving a negligible $p_{\text{null}} (< 10^{-10})$, indicating strong positive correlations. These relations are described well with linear functions: $T_{\text{seed}} = 0.59 + 0.15 F_{\text{UVW2}}$

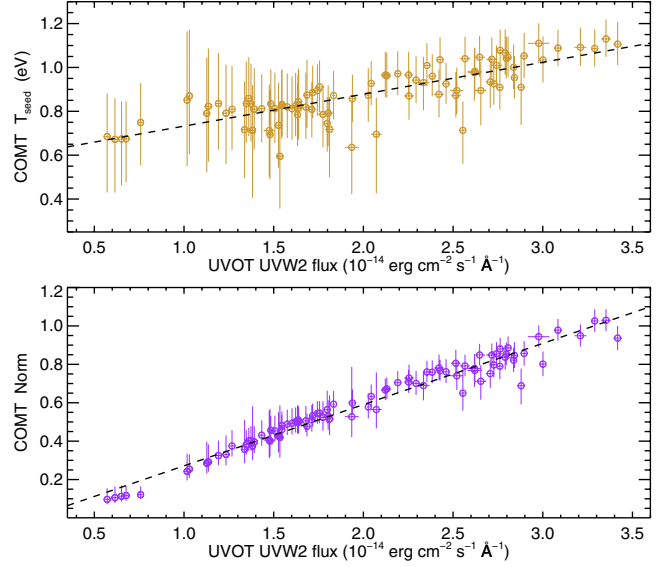


Fig. 6. *Top panel:* relation between the seed photon temperature T_{seed} of the comt (Comptonised optical-UV/soft X-ray excess) component and the observed UV flux in the *UVW2* filter. *Bottom panel:* relation between the normalisation of comt and the observed *UVW2* flux. The comt normalisation is shown in units of 10^{56} photons $\text{s}^{-1} \text{keV}^{-1}$. The data in the above panels have been fitted with linear functions, shown in dashed black lines, as described in Sect. 3.1.

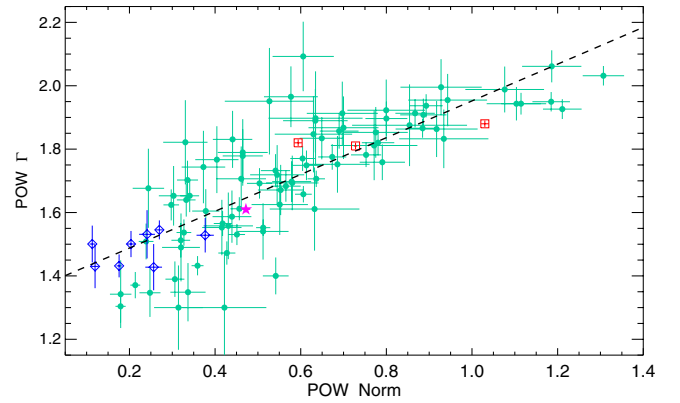


Fig. 7. Relation between the photon index Γ and the normalisation of the power-law (pow) continuum as described in Sect. 3.1. The pow normalisation is shown in units of 10^{52} photons $\text{s}^{-1} \text{keV}^{-1}$ at 1 keV. The data in green filled circles represent the *Swift* data from the obscured epoch (Feb. 2012 onwards), the blue open diamonds are the *Swift* data from the unobscured epoch of 2005 and 2007, the red open squares represent three *XMM-Newton* observations from unobscured epoch of 2000 and 2001, and the single filled magenta star corresponds to the stacked data from our summer 2013 campaign when the source was obscured. The data have been fitted with Eq. (3) shown in dashed black line.

and $N_{\text{comt}} = -0.047 + 0.32 F_{\text{UVW2}}$, where the unit of T_{seed} is in eV, N_{comt} in 10^{56} photons $\text{s}^{-1} \text{keV}^{-1}$ and the observed F_{UVW2} in $10^{-14} \text{erg cm}^{-2} \text{s}^{-1} \text{\AA}^{-1}$.

The parameter variability results of Fig. 4 also show that there is a relation between Γ and the normalisation of the power law (N_{pow}), with the power-law spectrum becoming softer as it gets brighter. In Fig. 7 we have plotted Γ versus the normalisation of the power law. In this figure, as well as the pow parameters derived from our modelling of the *Swift* data, we have also

shown the pow parameters from 2000 and 2001 *XMM-Newton* observations and from the stacked summer 2013 data of our campaign, obtained in Paper I. The correlation coefficient between N_{pow} and Γ is $r = 0.801$ for a sample size of 97, which gives a negligible $p_{\text{null}} (< 10^{-10})$, indicating a strong positive correlation. The data shown in Fig. 7 are fitted with the linear function

$$\Gamma = 1.37 + 0.58 N_{\text{pow}} \quad (3)$$

where normalisation N_{pow} is in units of 10^{52} photons s^{-1} keV^{-1} at 1 keV.

Finally, we note that there is a significant correlation between the UVW2 flux (F_{UVW2}) and the power-law parameters. For the sample size of 90, the correlation coefficient between F_{UVW2} and Γ is $r = 0.288$, and between F_{UVW2} and N_{pow} is $r = 0.645$. The corresponding null hypothesis probability for these correlations is $p_{\text{null}} = 0.0059$ and $p_{\text{null}} < 10^{-10}$, respectively, indicating positive correlations between the variability of the UV flux and the power-law component.

4. Broadband temporal rms variability analysis

In this section we use the *Swift* and HST COS lightcurves of NGC 5548 to determine the rms variability at different energies. The shape of an rms spectrum provides us with an important model-independent insight into the nature of variability. We can then compare the observed rms spectra of NGC 5548 with the model rms spectra generated from the results of our broadband spectral modelling in Sect. 3 (Fig. 4).

We calculated the fractional rms variability amplitude, following the recipe of Vaughan et al. (2003). For a series of N flux measurements of x_i , with a mean of \bar{x} , the fractional rms variability amplitude F_{var} is given by

$$F_{\text{var}} = \sqrt{\frac{\sigma_{\text{XS}}^2}{\bar{x}^2}} \quad (4)$$

where the excess variance $\sigma_{\text{XS}}^2 = S^2 - \overline{\sigma_{\text{err}}^2}$, the variance $S^2 = \sum_{i=1}^N (x_i - \bar{x})^2 / (N - 1)$ and $\overline{\sigma_{\text{err}}^2}$ is the mean square error on the count rate measurements. To compute the uncertainty of F_{var} , we used the prescription developed in Vaughan et al. (2003), which utilises Monte Carlo simulations to take into account the effects of flux measurement errors; see Eq. (11) and Appendix B in Vaughan et al. (2003) for more details. Time sampling bin size Δt_{bin} of ten days was selected for our computations to match the Δt_{bin} of our broadband spectral modelling in Sect. 3.

We calculated F_{var} for the NGC 5548 lightcurves at 25 different energy bins: 14 *Swift* XRT energy bins between 0.3–10 keV, the 6 UVOT photometric filters (*V*, *B*, *U*, *UVW1*, *UVM2* and *UVW2*) and the 5 HST COS continuum measurements from narrow wavelength bins in the UV (1158 Å, 1367 Å, 1462 Å, 1479 Å and 1746 Å). The rms variability spectra were calculated for lightcurves from two particular periods in 2013 and 2014: 26 April 2013 to 23 August 2013 and 8 February 2014 to 27 July 2014. These periods, which are indicated by the green vertical dotted lines in the panels of Fig. 4, were selected for two main reasons: (1) they correspond to the most intense and continuous *Swift* monitorings of NGC 5548, overlapping with the *XMM-Newton* campaign of 2013 and the HST COS monitoring programme of 2014 (thus also making the construction of COS rms variability spectra possible); (2) the results of our broadband spectral modelling in Fig. 4 suggest different variability

behaviour for key parameters during these two epochs, which are interesting to explore: the UV flux and the comt component display a more steady and larger increase over time in 2013 than in 2014; on the other hand, the obscurer C_f varies over a larger range in 2014 than in 2013. Thus, examining the differences in the shape of the observed rms variability spectra over these periods provides a useful model-independent signature for the nature of the variability, and we can check whether the observed rms spectra are consistent with our broadband modelling results.

Figure 8 shows the rms variability spectra of NGC 5548 for the selected periods in 2013 and 2014. In addition to the observed rms spectra from *Swift* and HST COS over the selected periods, we have over-plotted the model rms spectra generated from the results of our broadband spectral modelling in Sect. 3 (Fig. 4). The overall model rms spectrum (shown in black solid line in each panel) is calculated by letting all the free parameters of the model to vary within the observed best-fit values shown in Fig. 4 (i.e. the parameters of pow, comt, as well as the obscurer C_f). The overall model rms spectrum agrees well with the observed rms spectrum in both 2013 and 2014 periods, confirming that the results of our broadband spectral modelling in Sect. 3 matches our model-independent results from the rms variability analysis of the count rate lightcurves. Apart from the overall model rms spectra shown in Fig. 8, we have also derived the rms spectrum of individual components of our broadband spectral model (comt, pow and the obscurer C_f), which help us in visualising the spectral variability of these components. The rms spectrum for each component was calculated by fixing all the parameters of the model to that of the first observation in each period and then letting only the interested parameters (e.g. C_f) to vary according to the best-fit values obtained in Fig. 4. We note that the overall rms spectrum is not simply the sum of individual rms spectra of the components. Depending on how the individual parameters vary over time, their combined effect on the resulting rms spectrum can be different. The rms variability spectra of comt, pow and the obscurer C_f are displayed in Fig. 8.

The first striking difference between the observed rms spectra of 2013 (top panel) and 2014 (bottom panel) in Fig. 8 is the rms shape in the soft X-ray band between 0.3 and 1.0 keV. While in 2013 F_{var} is low in the soft X-ray band and displays a decline towards lower energies, during the 2014 period F_{var} is much higher with a steep rise towards lower energies. The second interesting difference between the two rms spectra is at optical-UV energies. While in both periods, F_{var} clearly displays a linear rise extending from optical to UV energies, the rise is steeper in the UV data of 2013 than in 2014. However, beyond the Lyman limit (13.6 eV), the model rms spectrum in 2014 rises very strongly towards EUV, similar to the rise from soft X-rays towards EUV energies.

The difference between the 2013 and 2014 observed rms spectra is due to the difference between the combined effect of the obscurer and continuum variability during these two periods. As evident in Fig. 8, the rms variability of the obscurer C_f is dominant over those of the continuum components in the EUV and soft X-ray energies in the 2014 period, whereas it is comparable to them in the 2013 period. Note that even small variations of C_f (such as in the 2013 period) still induce significant soft X-ray flux variability. In the 2013 period, the variability of the obscurer C_f (ranging from 0.92 to 0.97 in Fig. 4) and the comparable variability of the continuum components are such that their combined effect lowers the F_{var} amplitude of the overall rms spectrum. On the other hand, in the 2014 period, the stronger variability of the obscurer C_f (ranging from 0.70 to 0.95 in Fig. 4) and the relatively weaker variability of the

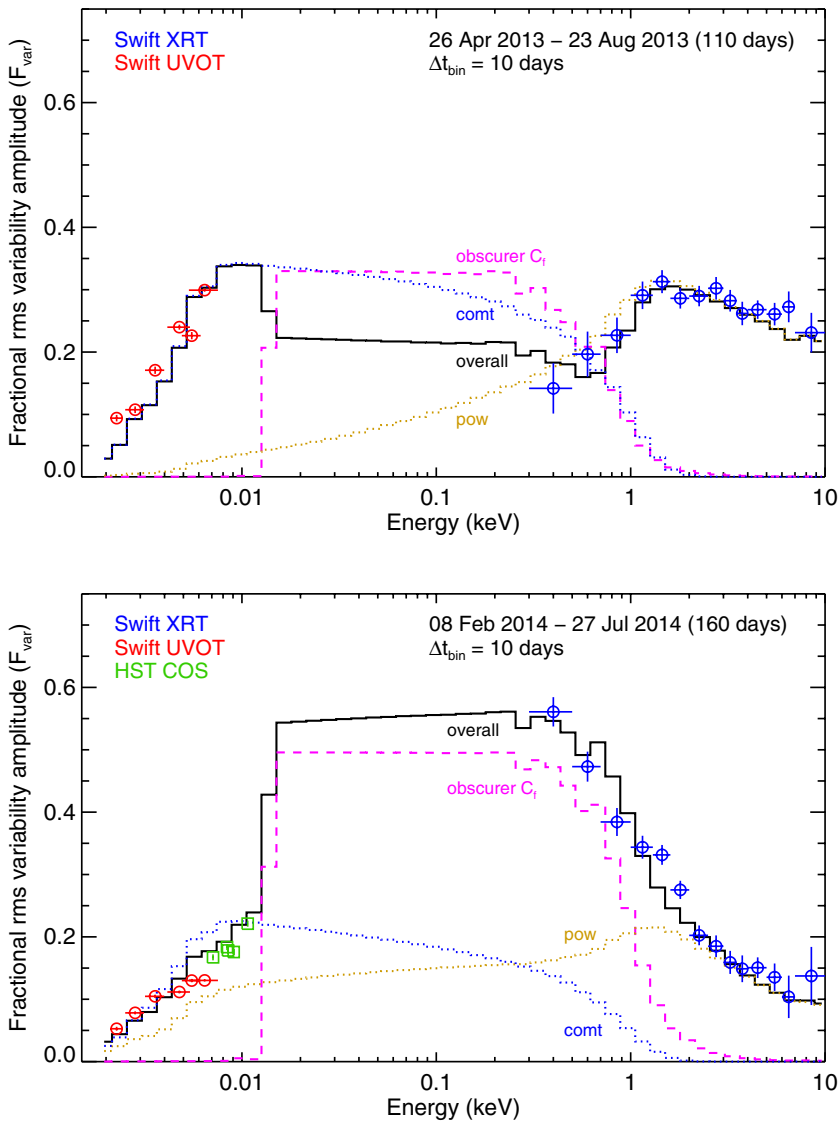


Fig. 8. *Swift* and HST COS broadband rms variability spectra of NGC 5548 for selected periods in 2013 (*top panel*) and 2014 (*bottom panel*). The XRT data are shown in blue circles and the UVOT data in red circles. The HST COS data (available only for the 2014 period) are displayed in green squares in the bottom panel. The overall rms variability model generated from the variability of all the parameters derived from our spectral modelling (Sect. 3 and Fig. 4) is over-plotted in solid black line on the data. The rms variability of individual model components are also over-plotted in the panels for comparison: comt in blue dotted line, pow in brown dotted line and the obscurer C_f in dashed magenta line. The calculation of the rms spectra are described in Sect. 4. The axes ranges in both panels are identical.

continuum components are such that they result in significant increase in the F_{var} amplitude of the overall rms spectrum in the EUV and soft X-ray energies. Therefore, depending on how the parameters vary over time, and any positive or negative correlations among them, their combined effect can result in a different overall rms spectrum. We note that in both the 2013 and 2014 periods, the overall model rms spectrum agrees well with the observed rms spectrum as seen in Fig. 8.

5. Discussion

5.1. Variability of the X-ray obscuring outflow in NGC 5548

In this investigation with *Swift* we have determined that the X-ray obscuring outflow in NGC 5548 is responsible for significant variability in the soft X-ray band on long timescales. The results of our broadband spectral modelling (Sect. 3, Fig. 4) and temporal rms variability analysis (Sect. 4, Fig. 8) show that this soft X-ray variability on timescales of 10 days to ~ 5 months can be explained by changes in the covering fraction C_f of the central X-ray source by the obscurer, which is located along our line of sight. We find that C_f has varied between 0.7 and nearly 1.0 over

the last few years, since the time *Swift* monitoring of NGC 5548 in the obscured state began in February 2012. The rms variability of the obscurer is found to be generally stronger than those of the power law and the warm Comptonisation component over the EUV and soft X-ray energies.

The *Swift* data point to the C_f of the obscurer being responsible for most of its long term variability. However, from analysis of the EPIC-pn data, Cappi et al. (2016) find that both the covering fraction C_f and column density N_H of the obscurer components can vary on shorter timescales of days to weeks. They find the rms variability produced by C_f of the warm component of the obscurer is stronger than the variability of other parameters of the obscurer. This is the same C_f parameter, which its variability is constrained with the *Swift* data on long timescales in this paper. The rms variability of other parameters of the obscurer are too subtle for detection and determination with *Swift* XRT due to its lower spectral resolution and effective area compared to EPIC-pn. We note that the N_H variability produces a bump with a characteristically sharp edge at 1 keV in the rms spectrum. However, this feature is not apparent in the *Swift* rms spectra, which may indicate a lack of significant N_H variability on long timescales.

To be able to study the obscuration phenomenon and its variability in NGC 5548, it is essential to separate the variability of the intrinsic continuum components from that of the obscurer as both can produce similar X-ray variability. In the soft X-ray band, the continuum of NGC 5548 is composed of an underlying power-law component (pow) with the addition of a soft X-ray excess component (comt). Thus, the variability of these two continuum components must be disentangled from that of the obscurer. This is achieved by broadband (optical-UV-X-ray) spectral modelling as performed in this paper. Since the soft excess component in NGC 5548 is consistent with being the high-energy tail of the optical-UV continuum as explained by warm Comptonisation (see [Paper I](#)), the optical-UV data of *Swift* UVOT and HST COS enable us to constrain the strength of the soft excess emission. Thus, we can separate emission variability of the soft excess from absorption variability of the obscurer. Also, the 2–10 keV part of the *Swift* XRT spectrum allows us to constrain the power-law component, thus the variability of the power law, the soft excess and the obscurer is determined.

The obscurer in NGC 5548, as well as heavily absorbing the soft X-rays, produces broad absorption lines (e.g. CIV) in the UV band (see [K14](#)), while hardly absorbing the UV continuum. From spectroscopy of these UV lines, it is found that the obscurer is outflowing with velocities of up to 5000 km s^{-1} . Therefore, some of the observed changes in C_f of the obscurer are likely to be associated with its patchy nature and high outflow velocity. The obscurer, as well as having an outflow velocity component in our line of sight, is also likely to have a transverse velocity component. Therefore, the motion of the obscuring gas in our line of sight, plus any inhomogeneities within it, can result in changes in the covering of the underlying X-ray source. Since the partially-covering obscuration in NGC 5548 has been persistent for at least 4 years and the *Swift* monitoring shows it has not yet cleared our line of sight since its discovery, this points to an outflowing structure with an elongated geometry, which most likely originates from the accretion disk given its close proximity to it. We note that there is currently an ongoing *Swift* monitoring of NGC 5548 on a monthly basis (ending June 2016) and these latest *Swift* data show that NGC 5548 is still obscured to this date (February 2016).

5.2. Nature of the optical-UV-X-ray continuum variability

The optical-UV continuum of NGC 5548 agrees with a single thermal Comptonised component, also producing the soft X-ray excess. This has been shown in [Paper I](#) from broadband spectral modelling of stacked 2013 HST, *XMM-Newton* and NuSTAR spectra, as well as archival *XMM-Newton* observations. This explanation is consistent with the results of our broadband spectral modelling of the *Swift* and HST COS data in this paper. In [Fig. 8](#) we showed that the shape of the observed rms spectrum variability, as seen by the *Swift* UVOT and HST COS, is consistent with the model rms spectrum variability produced by changes in the normalisation and T_{seed} of the warm Comptonisation (comt) component. The variability of comt can explain the optical-UV variability at all times in NGC 5548. However, in [Fig. 8](#) there are small differences between the observed and model rms variability in the optical-UV band. This is most likely due to variability of the strong AGN emission lines, including Fe II and the Balmer continuum, that fall in this band, and which their variability in the UVOT photometric filters were modelled as being only constant in our study. The emission from the BLR is known to be variable in NGC 5548, and in AGN in general, which is the

basis of reverberation-mapping techniques ([Peterson et al. 2004](#); [Cackett et al. 2015](#)). In our model, only optical-UV rms variability due to the variability of the continuum is considered, whereas the observed rms variability over a period of a few months also includes variability of the BLR emission.

Apart from variability of the comt component, there appears to be a long-term trend of power law Γ variability in NGC 5548 ([Figs. 4 and 7](#)), with Γ being significantly lower in 2013 than in 2012 and 2014. We note that this hardening of the power-law photon index in NGC 5548 does not have any apparent relation to the obscuration event. Low Γ values (~ 1.5) are found in data before NGC 5548 became obscured: e.g. the 2005 and 2007 *Swift* data ([Fig. 7](#)) and the 2000 *Chandra* data ([Yaqoob et al. 2001](#)).

[Figure 7](#) shows that the photon index of the power law becomes softer with increasing X-ray flux. We note that this behaviour was also found on shorter timescales by [Di Gesu et al. \(2015\)](#), as well as in previous X-ray monitorings of NGC 5548, such as with RXTE and ASCA by [Chiang et al. \(2000\)](#). This brightening of the power law as it gets softer is also found in similar Seyfert 1 AGN (e.g. NGC 7469, [Blustin et al. 2003](#); NGC 3516, [Mehdipour et al. 2010](#)), and most likely originates in changes in the Compton up-scattering by the hot, optically thin corona which produces the primary power-law emission ([Haardt & Maraschi 1993](#)). Basically, as the photon flux increases, more photons are scattered in the corona and so the corona loses energy, hence the steeper power law. The positive correlation between the variability of the UV flux and the power-law normalisation and Γ (found in [Sect. 3.1](#)) is also likely to be associated with the hot Comptonisation process. We note that in [Fig. 7](#), there is a possible indication that the power-law photon index stays unchanged at Γ of about 2 for power-law normalisations N_{POW} above $1 \times 10^{52} \text{ photons s}^{-1} \text{ keV}^{-1}$ at 1 keV. Such saturation of Γ has previously been interpreted to be a signature of bulk-motion Comptonisation flow onto the black hole by [Shaposhnikov & Titarchuk \(2009\)](#) and [Titarchuk & Seifina \(2016\)](#) in Galactic Black Hole Binaries.

Finally, in our *Swift* study of NGC 5548, we find that as the strength of the optical-UV/soft X-ray excess (comt) component increases during periods of UV flaring, the covering fraction C_f of the obscurer decreases. We note that in our modelling, only the normalisation and T_{seed} of comt, and C_f of the obscurer, were needed to fit the *Swift* and HST COS optical-UV/soft X-ray data. Thus, the impact of any smaller variation of other parameters, which were kept fixed in our modelling, is not known. However, in the analysis of *XMM-Newton* and *Chandra* data by [Di Gesu et al. \(2015\)](#), where both C_f and N_H of the obscurer were fitted, similar correlations to ours were found between the parameters. The limitations of the *Swift* data and the modelling are unlikely to be responsible for producing erroneous correlations as similar results are obtained across our papers studying different aspects of NGC 5548. Although in the soft X-ray band both comt and C_f can contribute to the rms spectral variability (as shown in [Fig. 8](#)), the strength of the comt component is primarily determined from the optical-UV flux. Note that the optical-UV continuum below the Lyman limit (13.6 eV) is unaffected by the obscuration. With simultaneous optical-UV data from UVOT and HST COS, it is possible to disentangle changes in the strength of the soft excess flux from the covering fraction C_f of the obscurer. Thus, the obtained anti-correlation is unlikely to be a mere artefact of spectral fitting. One possible explanation for this apparent anti-correlation between the covering fraction of the obscurer and the strength of the soft excess emission during UV flaring could be if the size of the soft excess emitting

coronal region in the inner regions of the disk varies. In this picture, as the area emitting the soft excess becomes larger (i.e. r_{corona} becomes larger), the nearby obscurer in our line of sight covers less of the X-ray emitting region. Hence, the observed C_f becomes smaller. The details of the corresponding decrease in C_f depend on the uncertain geometry of the stream of obscuring gas relative to the corona in our line of sight. However, in simple terms the new covering fraction would be approximately $C'_f \propto C_f (r_{\text{corona}}/r'_{\text{corona}})^2$.

6. Conclusions

We have studied the optical-UV-X-ray variability of Seyfert 1 galaxy NGC 5548 using remarkably extensive and intense monitoring campaigns with *Swift* and HST COS. By performing broadband modelling of the spectra and rms variability analysis of the lightcurves, we have disentangled intrinsic continuum variability from absorption variability of the obscuring outflow near the disk. From the findings of our investigation we conclude that:

1. The X-ray obscurer (which is composed of outflowing weakly-ionised gas extending from near the disk to the BLR) has been continuously present in our line of sight since at least February 2012. It has been partially covering the X-ray source since its discovery to this date, and has never cleared our line of sight. The *Swift* data show that NGC 5548 was unobscured in August 2007. However, due to lack of any monitoring between August 2007 and February 2012, it is not possible to more precisely determine when the transition between the unobscured and obscured states occurred.
2. The covering fraction of the obscurer is time variable, ranging between $0.70 \leq C_f \leq 0.98$. The observed X-ray hardness ratio (R) variability is predominantly caused by changes in the covering fraction of the obscurer. Some of the C_f changes are likely to be due to the transverse motion of the outflowing obscurer in our line of sight and its patchy nature. The persistence of such partially-covering and outflowing obscuration over several years indicates an outflowing structure with an elongated geometry.
3. Our analysis of the *Swift* data confirms that the soft X-ray excess in NGC 5548 is consistent with being the high-energy tail of the optical-UV continuum, which can be explained by warm Comptonisation: up-scattering of the disk seed photons in a warm, optically thick corona as part of the inner disk.
4. The *Swift* data reveal that when the optical-UV flux flares up (steep continuous increase over 1–2 months), the hardness ratio R and the obscurer C_f become smaller. This may imply that as the optical-UV/soft excess emitting warm corona on the surface of the disk becomes larger during these periods, the obscurer stream covers less of the X-ray source.

Acknowledgements. This work made use of data supplied by the UK Swift Science Data Centre at the University of Leicester. SRON is supported financially by NWO, the Netherlands Organization for Scientific Research. M.M. acknowledges support from NWO and the UK STFC. This work was supported by NASA through grants for HST programme number 13184 from the Space Telescope Science Institute, which is operated by the Association of Universities for Research in Astronomy, Incorporated, under NASA contract NAS5-26555. M.C. acknowledges financial support from contracts ASI/INAF n.I/037/12/0 and PRIN INAF 2011 and 2012. P.-O.P. acknowledges financial support from the CNES and from the CNRS/PICS. G.P. acknowledges support via an EU Marie Curie Intra-European fellowship under contract no. FP-PEOPLE-2012-IEF-331095 and Bundesministerium für Wirtschaft und Technologie/Deutsches Zentrum für Luft- und Raumfahrt (BMW/DLR, FKZ 50 OR 1408). K.C.S. acknowledges financial support from the Fondo Fortalecimiento de la Productividad Científica VRIDT 2013. E.B. received funding from the EU Horizon 2020 research and innovation programme under the Marie Skłodowska-Curie grant agreement No. 655324, and from the I-CORE programme of the Planning and Budgeting Committee (grant number 1937/12). S.B. and G.M. acknowledge INAF/PICS financial support. G.M. and F.U. acknowledge financial support from the Italian Space Agency under grant ASI/INAF I/037/12/0-011/13. B.M.P. acknowledges support from the US NSF through grant AST-1008882. F.U. acknowledges Ph.D. funding from the VINCI programme of the French-Italian University. M.W. acknowledges the support of a Ph.D. studentship awarded by the UK Science & Technology Facilities Council (STFC). We thank the International Space Science Institute (ISSI) in Bern for their support and hospitality. We thank the anonymous referee for the useful comments.

References

- Blustin, A. J., Branduardi-Raymont, G., Behar, E., et al. 2003, *A&A*, **403**, 481
 Burrows, D. N., Hill, J. E., Nousek, J. A., et al. 2005, *Space Sci. Rev.*, **120**, 165
 Cackett, E. M., Gültekin, K., Bentz, M. C., et al. 2015, *ApJ*, **810**, 86
 Cappi, M., De Marco, B., Ponti, G., et al. 2016, *A&A*, submitted (Paper VIII)
 Chiang, J., Reynolds, C. S., Blaes, O. M., et al. 2000, *ApJ*, **528**, 292
 De Rosa, G., Peterson, B. M., Ely, J., et al. 2015, *ApJ*, **806**, 128
 de Vaucouleurs, G., de Vaucouleurs, A., Corwin, Jr., H. G., et al. 1991, Third Reference Catalogue of Bright Galaxies, Volume I, Explanations and references, Volume II, Data for galaxies between 0h and 12h, Volume III, Data for galaxies between 12h and 24h (New York: Springer)
 Di Gesu, L., Costantini, E., Ebrero, J., et al. 2015, *A&A*, **579**, A42
 Done, C., Davis, S. W., Jin, C., Blaes, O., & Ward, M. 2012, *MNRAS*, **420**, 1848
 Fabian, A. C. 2012, *ARA&A*, **50**, 455
 Ferland, G. J., Korista, K. T., Verner, D. A., et al. 1998, *PASP*, **110**, 761
 Gehrels, N., Chincarini, G., Giommi, P., et al. 2004, *ApJ*, **611**, 1005
 Green, J. C., Froning, C. S., Osterman, S., et al. 2012, *ApJ*, **744**, 60
 Haardt, F., & Maraschi, L. 1993, *ApJ*, **413**, 507
 Kaastra, J. S., Mewe, R., & Nieuwenhuijzen, H. 1996, in *UV and X-ray Spectroscopy of Astrophysical and Laboratory Plasmas*, eds. K. Yamashita, & T. Watanabe (Tokyo: Universal Academic Press Inc.), 411
 Kaastra, J. S., Detmers, R. G., Mehdipour, M., et al. 2012, *A&A*, **539**, A117
 Kaastra, J. S., Kriss, G. A., Cappi, M., et al. 2014, *Science*, **345**, 64 (K14)
 Mehdipour, M., Branduardi-Raymont, G., & Page, M. J. 2010, *A&A*, **514**, A100
 Mehdipour, M., Kaastra, J. S., Kriss, G. A., et al. 2015, *A&A*, **575**, A22 (Paper I)
 Peterson, B. M., Ferrarese, L., Gilbert, K. M., et al. 2004, *ApJ*, **613**, 682
 Petrucci, P. O., Haardt, F., Maraschi, L., et al. 2000, *ApJ*, **540**, 131
 Proga, D., & Kallman, T. R. 2004, *ApJ*, **616**, 688
 Proga, D., Stone, J. M., & Kallman, T. R. 2000, *ApJ*, **543**, 686
 Roming, P. W. A., Kennedy, T. E., Mason, K. O., et al. 2005, *Space Sci. Rev.*, **120**, 95
 Shaposhnikov, N., & Titarchuk, L. 2009, *ApJ*, **699**, 453
 Steenbrugge, K. C., Kaastra, J. S., Crenshaw, D. M., et al. 2005, *A&A*, **434**, 569
 Sunyaev, R. A., & Titarchuk, L. G. 1980, *A&A*, **86**, 121
 Tarter, C. B., Tucker, W. H., & Salpeter, E. E. 1969, *ApJ*, **156**, 943
 Titarchuk, L., & Seifina, E. 2016, *A&A*, **585**, A94
 Ursini, F., Boissay, R., Petrucci, P.-O., et al. 2015, *A&A*, **577**, A38
 Vaughan, S., Edelson, R., Warwick, R. S., & Uttley, P. 2003, *MNRAS*, **345**, 1271
 Yaqoob, T., George, I. M., Nandra, K., et al. 2001, *ApJ*, **546**, 759

Appendix A: Relations between the optical and UV lightcurves of NGC 5548

Figure A.1 shows how the optical and UV fluxes taken in the *Swift* UVOT photometric filters are related to each other. From fitting the flux in different filters versus the flux in the *UVW2* filter, we derive the following empirical relations (in units of $10^{-14} \text{ erg cm}^{-2} \text{ s}^{-1} \text{ \AA}^{-1}$) described by quadratic functions

$$F_V = 0.512 + (0.354 F_{UVW2}) - (0.037 F_{UVW2}^2) \quad (\text{A.1a})$$

$$F_B = 0.312 + (0.545 F_{UVW2}) - (0.050 F_{UVW2}^2) \quad (\text{A.1b})$$

$$F_U = -0.039 + (1.132 F_{UVW2}) - (0.101 F_{UVW2}^2) \quad (\text{A.1c})$$

$$F_{UVW1} = 0.039 + (1.238 F_{UVW2}) - (0.084 F_{UVW2}^2) \quad (\text{A.1d})$$

$$F_{UVM2} = -0.042 + (1.123 F_{UVW2}) - (0.034 F_{UVW2}^2). \quad (\text{A.1e})$$

We note that the UVOT flux values in the above relations are the observed flux and do not necessarily represent the flux of the continuum. They include flux contributions from the BLR, the NLR and the host galaxy stellar emission, as well as Galactic reddening, which are all taken into account separately during the spectral fitting in SPEX using the optical/UV correcting components reported in Paper I. The above empirical relations have been used to calculate the observed UVOT flux for those *Swift* observations when exposures in some of the six UVOT filters have not been taken. This method is useful in the context of broadband spectral modelling of the *Swift* data, as it provides us with the same number of data sets (covering identical energy bands) in all the *Swift* observations, in order to carry out a uniform and consistent spectral fitting of the data.

In Fig. A.2 we show the flux relations between the contemporaneous HST COS and UVOT *UVW2* observations (separated by less than 24 h). From fitting the COS continuum flux at different wavelengths versus the *UVW2* filter flux, we derive the following empirical relations (in units of $10^{-14} \text{ erg cm}^{-2} \text{ s}^{-1} \text{ \AA}^{-1}$) described by quadratic functions

$$F_{1158 \text{ \AA}} = -2.249 + (1.992 F_{UVW2}) + (0.155 F_{UVW2}^2) \quad (\text{A.2a})$$

$$F_{1367 \text{ \AA}} = -1.235 + (1.811 F_{UVW2}) + (0.076 F_{UVW2}^2) \quad (\text{A.2b})$$

$$F_{1462 \text{ \AA}} = -0.649 + (1.235 F_{UVW2}) + (0.157 F_{UVW2}^2) \quad (\text{A.2c})$$

$$F_{1479 \text{ \AA}} = -1.464 + (1.770 F_{UVW2}) + (0.067 F_{UVW2}^2) \quad (\text{A.2d})$$

$$F_{1746 \text{ \AA}} = -1.072 + (1.576 F_{UVW2}) + (0.025 F_{UVW2}^2). \quad (\text{A.2e})$$

The observed COS fluxes in the above relations include the Galactic reddening and are from five narrow energy bands, which are free of emission and absorption features to represent the continuum. The above relations were used to calculate the COS continuum fluxes for those *Swift* observations without contemporaneous HST COS data. These predicted COS fluxes were used in our broadband spectral modelling in order to constrain the far-UV continuum.

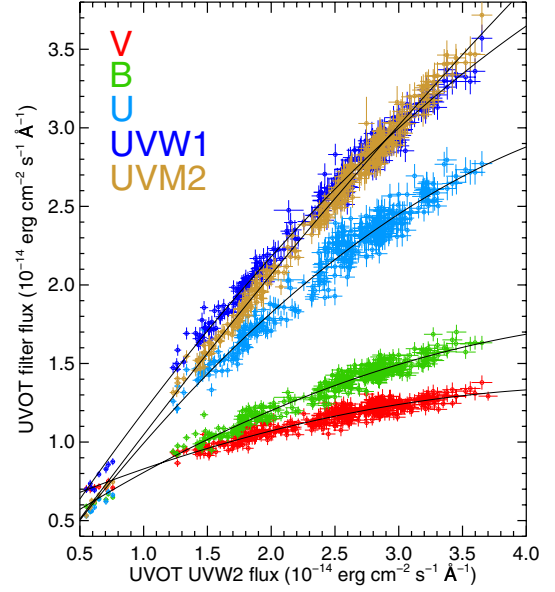


Fig. A.1. Relations between the observed optical and UV fluxes of NGC 5548 taken with the six photometric filters of *Swift* UVOT. The fitted functions are given in Eqs. (A.1).

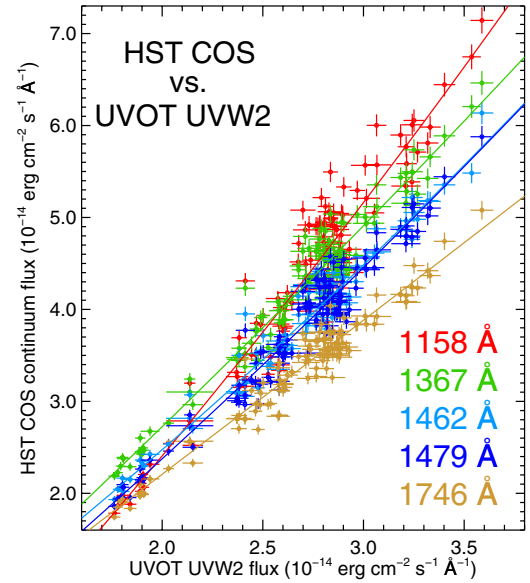


Fig. A.2. HST COS continuum fluxes of NGC 5548 plotted versus contemporaneous UVOT *UVW2* flux. The observed COS fluxes are taken from five narrow energy bands, which are free of emission and absorption features to represent the continuum. The fitted functions are given in Eqs. (A.2).